Architecture of Sintered-Regolith Lunar Polar Microhabitats for Biofilm Research

Miguel Angel Vargas Cruz

Grupo Alianza Empresarial: Mexico City, Mexico

Abstract

This paper presents a parametric design framework for sintered-regolith microhabitats at the lunar poles and couples it to a reduced model of biofilm attachment, growth, and radiative damage on internal liner materials. The workflow integrates polar illumination geometry derived from Lunar Orbiter Laser Altimeter (LOLA) digital elevation models, regolith thermophysical constraints from the Diviner Lunar Radiometer Experiment (Diviner) and sintering studies, and microbiological priors derived from International Space Station (ISS) datasets, including OSD-554. Spherical-cap shells are parameterized by base radius, rise, and thickness; horizon masks provide fractional illumination; a one-dimensional multilayer spherical-conduction model defines thermal screening variables; and normalized sintering-energy and biofilm-control metrics support multiobjective comparison. The biological model is explicitly treated as a finite-horizon screening model rather than an experimentally calibrated predictor. For the parameter sets used here, the analytical transition from positive to negative net biofilm growth occurs at normalized internal ultraviolet (UV) doses of approximately 0.396127 for a stainless-steel-like liner and 0.052941 for a liquid-infused-surface-like liner. One-at-a-time perturbations of the biological parameters quantify the uncertainty of these thresholds, while normalized shell-energy scaling shows the expected quadratic dependence on base radius and linear dependence on thickness. The results support relative ranking of materials, sites, and geometries, but not mission-level prediction. Complete source code and execution instructions are provided externally to preserve manuscript readability and reproducibility.

Keywords:

lunar architecture; sintered regolith; polar illumination; thermal modeling; biofilm control; reproducible computation

List of Abbreviations

AI	Artificial Intelligence
BAC	Bacterial Adhesion and Corrosion
Diviner	Diviner Lunar Radiometer Experiment
EPS	Extracellular Polymeric Substance
HTML	Hypertext Markup Language
ISRU	In Situ Resource Utilization
ISS	International Space Station
LIS	Liquid-Infused Surface
LOLA	Lunar Orbiter Laser Altimeter
LRO	Lunar Reconnaissance Orbiter
LROC	Lunar Reconnaissance Orbiter Camera
ML	Machine Learning
NASA	National Aeronautics and Space Administration
ODE	Ordinary Differential Equation
OSD-554	OSDR study accession 554
OSDR	Open Science Data Repository
PDS	Planetary Data System
PSR	Permanently Shadowed Region
SS	Stainless Steel
UV	Ultraviolet
UVC	Ultraviolet C
UV-LED	Ultraviolet-C Light-Emitting Diode

1. Introduction

Future lunar surface architectures, particularly at the polar regions, must simultaneously satisfy three tightly coupled constraints: (i) power availability under highly anisotropic, seasonally modulated illumination; (ii) thermal management in the presence of steep radiative gradients and per-

* Corresponding Author:
Miguel Angel Vargas Cruz, Grupo Alianza Empresarial,
miguelangel@grupoalianzaempresarial.com

manently shadowed regions (PSRs); and (iii) mechanical robustness and constructability using in situ resources. Long-baseline simulations with Lunar Orbiter Laser Altimeter (LOLA) topography have shown that only a small fraction of polar terrain achieves near-continuous or quasi-continuous illumination over a precessional cycle [1,2], while radiometry from the Diviner Lunar Radiometer Experiment (Diviner) reveals strong spatial variability in regolith thermophysical properties that governs diurnal and seasonal temperature swings [3]. These constraints are particularly acute along narrow ridges and crater rims where illumination, access to PSRs, and engineering feasibility must be traded against each other. In parallel, the National Aeronautics and Space Administration (NASA) Open Science Data Repository (OSDR) has emerged as an open-science model for spaceflight biology, curating space-flown and ground-based analogue datasets and demonstrating how multiomics, physiological, and imaging data from low-sample-size missions can be integrated to advance biofilm biology and enable artificial intelligence (AI) and machine learning (ML) analysis pipelines [6].

In situ resource utilization (ISRU) has progressed from conceptual studies to experimental demonstrations of solar-driven sintering and additive manufacturing with lunar regolith simulants. Concentrated sunlight has been used to fabricate three-dimensional bricks and structural elements by directly sintering regolith layers, without imported binders [5]. Recent reviews of lunar regolith forming technologies emphasize that sintered or cast regolith could provide radiation shielding, structural shells, and thermal mass for surface infrastructure, provided that process windows and mechanical properties can be reliably controlled under lunar conditions [4]. These developments motivate microhabitat concepts in which thin, sintered shells act as structural and radiative envelopes, while internal liners and inserts host functional subsystems.

Against this background, microbial life is not an optional add-on but an intrinsic component of any long-duration human presence in space. Biofilms (surface-associated, matrix-embedded microbial communities) are now recognized as a dominant mode of microbial life on Earth and an important contributor to the early fossil record [6]. In the context of spaceflight, environmental surveys and longitudinal studies at the International Space Station (ISS) have shown that confined habitats develop characteristic microbiomes shaped by crew, materials, and operational patterns [7,9]. Reviews focused on biofilms in space highlight that biofilm formation can compromise hardware, alter corrosion and fouling of stainless-steel components, and modulate health risks for the crew, while also offering potential benefits for bioprocesses and life-support functions [8,10].

Targeted spaceflight experiments have begun to probe biofilm formation under microgravity and spacecraft-relevant conditions. The Space Biofilms project and the Bacterial Adhesion and Corrosion (BAC) investigations examine how mono- and polymicrobial biofilms grow on stainless steel, respond to microgravity, and interact with candidate biocides and surface treatments, using organisms such as *Pseudomonas aeruginosa* and *Penicillium rubens* as model systems [11,12]. These datasets provide quantitative constraints on attachment rates, extracellular polymeric substance (EPS) production, stress-response pathways, and material-specific differences in colonization that are directly relevant to engineered surfaces in space habitats.

The present work explores a deliberately constrained problem at the intersection of these domains: the design space of sintered-regolith microhabitats whose internal surfaces serve as controlled interfaces for biofilm formation and suppression. Rather than proposing a full-scale habitat architecture, we focus on a single class of geometries (spherical-cap sandwich shells) anchored to polar ridge sites with favorable illumination and regolith properties. We then couple: (i) a generative geometric model that produces a family of shells parameterized by radius, height, and thickness; (ii) a one-dimensional radial conduction model that evaluates internal climate under polar forcing; and (iii) a reduced biofilm model that maps an illumination-coupled, engineered internal ultraviolet (UV) control variable and material properties into a finite-horizon biofilm response and a scalar controllability index.

The goal is not to produce operational design recommendations, but to construct a computational scaffold that links open planetary and microbiological measurements to architecturally legible variables. The framework is therefore evaluated as a conceptual and exploratory screening system. Its outputs are benchmarked against published ranges and qualitative material ordering, and its sensitivity to the principal assumptions is quantified; however, no claim of experimental calibration, structural qualification, or mission readiness is made. By explicitly tracing the mapping from LOLA/Diviner/Lunar Reconnaissance Orbiter Camera (LROC) products and ISS biofilm experiments into effective biofilm and thermophysical parameters, the analysis identifies which combinations of site, shell geometry, liner treatment, and controlled internal UV exposure warrant higher-fidelity simulation or laboratory validation.

2. Methods

2.1. Geometry and generative model

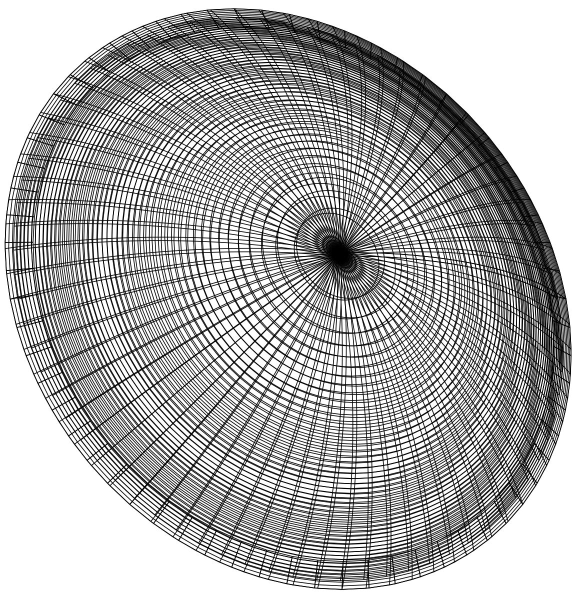

Figure 1: Parametric spherical-cap shell used as the geometric abstraction for the microhabitat. The complete geometry generator is available through the external code archive described in Section 2.9.

The microhabitat is represented as a spherical-cap sandwich shell with base radius R, rise h, structural thickness t, rim width w, and rim rise w_r (Figure 1). This abstraction is consistent with classical thin-shell formulations and recent finite-element verification studies of spherical domes [13,14]; no structural qualification is claimed here. The radius of curvature of the outer cap is

$$S_o = \frac{R^2 + h^2}{2h}, \tag{1}$$

and the cap terminates at

$$\theta_{\text{max}} = \arcsin\left(\frac{R}{S_o}\right). \tag{2}$$

The inner surface is generated by the reduced dimensions $R_i = R - t$ and $h_i = h - t$, giving

$$S_i = \frac{R_i^2 + h_i^2}{2h_i}. \tag{3}$$

This notation removes the previous ambiguity between the base radius and the radius of curvature. The outer and inner meshes are sampled over meridional and azimuthal coordinates and exported as a watertight triangulated object for inspection and downstream analysis. Local stiffeners, apertures, seals, tie-down hardware, and pressure-vessel details are excluded because the model represents a robotic experimental microhabitat rather than a crew-rated habitat.

For thin shells, the cap area and first-order shell volume are

$$A_{\text{cap}} = 2\pi S_o h = \pi(R^2 + h^2), \tag{4}$$
$$V_{\text{shell}} \simeq A_{\text{cap}} t. \tag{5}$$

The corresponding mass and sintering energy scale as

$$E_{\text{sint}} \simeq E_s \rho_{\text{reg}} \pi(R^2 + h^2)t, \tag{6}$$

where E_s is the effective specific process energy and ρ_{reg} is the processed-regolith density. Equation (6) is used only for normalized geometry sensitivity; detailed process planning would require toolpath, heat-loss, porosity, and rejected-material terms.

2.2. Site screening and horizon-based polar illumination

Let $z(\mathbf{x})$ denote a local LOLA digital elevation model. For a candidate point $\mathbf{x}_0$, the azimuthal horizon elevation is

$$\eta(\psi) = \max_{r \in [r_{\text{min}}, r_{\text{max}}]} \arctan\left[\frac{z(\mathbf{x}_0 + r\hat{\mathbf{e}}_\psi) - z(\mathbf{x}_0)}{r}\right], \tag{7}$$

where $\hat{\mathbf{e}}_\psi = (\cos\psi, \sin\psi)$. The radial maximum-slope construction follows established horizon-based polar illumination methods [1,17–20].

Near the lunar poles, the reduced solar-elevation track is represented as

$$\alpha(\psi; \theta_q) = |90^\circ - |\phi|| - \varepsilon \cos(\psi + \theta_q), \tag{8}$$

where $\varepsilon = 1.54^\circ$ and θ_q samples the slow precessional phase. Visibility is

$$v(\psi; \theta_q) = \begin{cases} 1, & \alpha(\psi; \theta_q) > \eta(\psi) + \delta, \\ 0, & \text{otherwise}, \end{cases} \tag{9}$$

with a safety margin $\delta = 0.1^\circ$. Fractional illumination is

$$f_{\text{illum}} = \frac{1}{QN_\psi} \sum_{q=1}^{Q} \sum_{j=1}^{N_\psi} v(\psi_j; \theta_q). \tag{10}$$

The reduced solar track omits libration, finite-disc integration, detailed ephemerides, and time-dependent terrain shadowing. It is used for relative site ranking, not for operational power prediction.

Candidate pixels are pre-filtered by slope and local relief. A typical evaluation uses $N_\psi = 720$, a radial search of up to 10 km, and eight precessional phases. The computational complexity is $\mathcal{O}(N_\psi N_r)$ per site. LOLA, Diviner, and LROC products provide topographic, thermophysical, and local-context constraints, respectively [3,22,23].

2.3. Radial thermal model and internal climate

The shell is reduced to L concentric spherical layers representing sintered regolith, bulk regolith, liner, and internal protective layers. In layer i,

$$\frac{\partial T_i}{\partial t} = \alpha_i(T)\left(\frac{\partial^2 T_i}{\partial r^2} + \frac{2}{r}\frac{\partial T_i}{\partial r}\right), \qquad r \in [r_{i-1}, r_i], \tag{11}$$

where $\alpha_i(T) = k_i(T)/(\rho_i c_{p,i}(T))$. The factor $2/r$ is required for spherical symmetry. Temperature and heat flux are continuous at every material interface. The interior and exterior boundary conditions are

$$-k\frac{\partial T}{\partial r}\bigg|_{r=r_0} = h_{\text{int}}[T(r_0,t) - T_{\text{int}}], \tag{12}$$

$$-k\frac{\partial T}{\partial r}\bigg|_{r=r_L} = q_\odot(t) - \epsilon\sigma\left[T(r_L,t)^4 - T_{\text{bg}}^4\right]. \tag{13}$$

The absorbed external flux is

$$q_\odot(t) = (1-\alpha_{\text{bol}})S_\odot v_\odot(t), \tag{14}$$

where α_{bol} is bolometric albedo. The previous notation, in which albedo multiplied the incident solar flux directly, has been corrected. Exterior radiation may be linearized around T_{ref} for implicit time integration. The radial discretization produces a tridiagonal system solved by an implicit or Crank–Nicolson scheme. Material properties are constrained by Diviner-derived behavior and laboratory measurements of regolith and sintered simulants [3,15,16, 21,24].

For first-order sensitivity, the thin-layer thermal resistance is

$$R_{\text{th}} \simeq \frac{t}{kA_{\text{cap}}}, \tag{15}$$

so the conductive temperature drop obeys $\Delta T \propto qt/k$. This scaling is used to quantify the direction and magnitude of uncertainty before three-dimensional analysis.

2.4. Sintering energy and autonomous construction

For processed mass m, total energy is

$$E_{\text{tot}} = E_s m. \tag{16}$$

Published microwave and solar-sintering studies span approximately 3×10^3–2×10^4 J g^{-1}, depending on peak temperature, coupling efficiency, porosity, and process path [5,25–29]. Available power is represented as

$$P_{\text{avail}} = \eta_{\text{conv}}\eta_{\text{point}}\eta_{\text{dust}}f_{\text{illum}}A_{\text{aperture}}S_\odot, \tag{17}$$

where the efficiency factors describe conversion, pointing, and dust derating. These factors are held constant in the present screening analysis. Robotic emplacement, excavation, feedstock grading, layer bonding, dust accumulation, maintenance, and repeated thermal cycling are not dynamically modeled.

2.5. Biofilm attachment and growth under controlled radiative stress

The biological subsystem retains the original two-state structure:

$$\frac{dA}{dt} = k_a\Phi_0 C_b - (k_d + \beta_\phi D_{\text{uv}})A, \tag{18}$$

$$\frac{dB}{dt} = \left[\mu_{\max}\frac{A}{K_s + A} - (k_d + \beta_\phi D_{\text{uv}})\right]B, \tag{19}$$

where A is attached biomass, B is biofilm biomass, C_b is a fixed planktonic-source proxy, k_a is a baseline attachment coefficient, k_d is an effective detachment/death rate, Φ_0 is a material-dependent attachment factor, $\mu_{\max}$ is a maximum specific growth rate, and $\beta_\phi D_{\text{uv}}$ is the effective radiative-damage rate. The model follows low-order attachment and Monod-type formulations but intentionally omits substrate depletion, carrying capacity, multispecies interactions, flow, EPS mechanics, mutation, and spatial gradients [30–33].

The normalized internal dose is

$$D_{\text{uv}} = \chi_{\text{uv}} f_{\text{illum}}, \tag{20}$$

where χ_{uv} combines engineered UV delivery, duty cycle, optical attenuation, shielding, and geometry. The baseline scenario uses $\chi_{\text{uv}} = 1$. Equation (20) does not imply that exterior lunar UV directly irradiates the internal liner; the microhabitat is assumed to contain a controlled UV source or an optically managed exposure path. Consequently, D_{uv} is dimensionless and cannot be compared directly with a laboratory fluence in mJ cm^{-2} without independent radiometric calibration.

For fixed D_{uv}, attached biomass converges to

$$A^* = \frac{k_a \Phi_0 C_b}{k_d + \beta_\phi D_{\text{uv}}}. \tag{21}$$

The asymptotic net growth exponent for B is

$$\lambda_B(D_{\text{uv}}) = \mu_{\max} \frac{A^*}{K_s + A^*} - (k_d + \beta_\phi D_{\text{uv}}). \tag{22}$$

Because Equation (19) is linear in B, it has no finite positive biomass equilibrium when $\lambda_B > 0$. The previously used term "steady-state biomass" is therefore replaced by the finite-horizon terminal-window metric

$$\begin{aligned} \overline{B}_T &= \frac{1}{N_T} \sum_{n \in \mathcal{I}_T} B(t_n), \\ \mathcal{I}_T &= \{n : t_n \geq 0.9T\}, \\ N_T &= 241, \end{aligned} \tag{23}$$

where $T = 240$ h, $t_n = n\Delta t$, and $\Delta t = 0.1$ h. Thus, the reported terminal-window value is the arithmetic mean of the 241 numerical samples from 216.0 through 240.0 h, inclusive. The same definition is used for $\overline{A}_T$. This correction preserves the model dynamics while preventing finite-time exponential growth from being misidentified as a biological steady state. The critical dose D_c is defined by $\lambda_B(D_c) = 0$.

2.6. Translation of OSD-554 data into biological priors

The OSD-554 normalized-count tables for stainless-steel-like (SS) and liquid-infused-surface-like (LIS) coupons are separated into flight and ground replicates [11]. For each material, the pipeline computes gene-wise $\log_2$ fold changes between flight and ground means, selects the ten genes with the largest absolute fold changes, and defines a condition score s_c as the mean normalized expression of those genes. Scores are standardized across the four gravity–material conditions:

$$z_c = \frac{s_c - \overline{s}}{\sigma_s}. \tag{24}$$

The standardized score is mapped monotonically to effective parameters:

$$\begin{aligned} \mu_{\max,c} &= 0.5(1 + 0.15 z_c), & (25)\\ k_{d,c} &= 0.05 \exp(-0.5 z_c), & (26)\\ \Phi_{0,c} &= 1 + 0.5 z_c, & (27)\\ \beta_{\phi,c} &= \exp(-0.3 z_c). & (28) \end{aligned}$$

The rates are expressed in h^{-1} where applicable. Equation (28) is a heuristic rank-preserving prior transformation, not a statistical or mechanistic calibration. It encodes the relative ordering present in the selected transcriptomic score and the experimentally observed tendency of LIS-like surfaces to reduce attachment relative to stainless steel [10,12].

Table 1: Effective microgravity parameter sets used in the reported comparison. Values are generated by the explicit score-to-parameter mapping in Equation (28); they are computational priors rather than experimentally measured kinetic constants.

Parameter	micro_SS	micro_LIS
$\mu_{\max}$ (h^{-1})	0.627	0.444
k_d (h^{-1})	0.0215	0.0724
Φ_0	1.845	0.629
β_ϕ (h^{-1} dose^{-1})	0.602	1.249

2.7. Trade-off indices and sensitivity protocol

The physical screening variables are

$$\Pi_{\text{illum}} = f_{\text{illum}}, \tag{29}$$

$$\Pi_{\text{sint}} = \frac{E_{\text{tot}}}{P_{\text{avail}} \tau}, \tag{30}$$

$$\Pi_{\text{therm}} = \frac{\Delta T_{\text{shell}}}{T_{\text{int}}}. \tag{31}$$

The biofilm controllability index retains the original comparative definition,

$$\mathcal{C}_{\text{bio}} = 1 - \frac{\overline{B}_T}{B_{\text{ref}}}, \tag{32}$$

where B_{ref} is the largest $\overline{B}_T$ within the explicitly stated comparison set. Because this normalization can saturate when all compared biomasses are very small, $\log_{10} \overline{B}_T$ and the critical dose D_c are reported alongside $\mathcal{C}_{\text{bio}}$.

A composite score may be formed as

$$\mathcal{S} = w_1 \Pi_{\text{illum}} - w_2 \Pi_{\text{sint}} - w_3 \Pi_{\text{therm}} + w_4 \mathcal{C}_{\text{bio}}, \tag{33}$$

but no universal weights are asserted. The present revision emphasizes Pareto structure and one-at-a-time sensitivity rather than a single preferred ranking. Biological parameters are perturbed by $\pm 20\%$ and the resulting D_c is recomputed. Thermal scaling is evaluated for $\pm 25\%$ perturbations in shell thickness, conductivity, and imposed heat flux. Geometry-energy sensitivity follows Equation (6).

2.8. Verification hierarchy and scope of validation

The framework uses four levels of verification. First, the geometry is checked against the analytical spherical-cap area and volume relations. Second, illumination outputs are compared with the range and spatial scarcity of highly illuminated polar ridges reported by LOLA-based studies [1,2,18,20]. Third, the radial thermal solver is checked against analytical steady spherical conduction and energy-balance limits before application to temperature-dependent properties. Fourth, biological outputs are checked for numerical convergence, analytical consistency with Equations (22)–(23), and qualitative SS–LIS ordering reported in ISS-relevant studies [10–12].

These checks establish internal consistency and literature correspondence, not experimental validation under simulated lunar conditions. A definitive validation campaign would require controlled measurements of SS and LIS coupons under specified nutrient, humidity, temperature, microgravity analogue, and calibrated UV fluence, followed by estimation of k_a, k_d, $\mu_{\max}$, and β_ϕ from replicated time-series data.

2.9. Software, reproducibility, and data

The complete Hypertext Markup Language (HTML) for the parametric shell renderer and Python source code (LOLA preprocessing, horizon and illumination analysis, OSD-554 prior construction, finite-horizon biofilm integration, controllability-index calculation, and dose-response sweep), execution sequence, and module descriptions are available in the external reproducibility archive [40].

3. Results

3.1. Benchmark correspondence

The selected polar candidate is the grid cell at row 197 and column 75, with $f_{\text{illum}} = 0.755556$. This value lies in the high-illumination regime used to screen narrow polar ridges and is consistent with the conclusion of long-baseline LOLA studies that such conditions occur only over a small fraction of polar terrain [1,2,18]. This comparison is a correspondence benchmark; the reduced solar-track model does not replace full ephemeris-based illumination analysis.

The biological parameter transformation reproduces the expected material ordering: the SS-like condition has a larger attachment factor and smaller effective detachment/damage coefficients than the LIS-like condition (Table 1). This is consistent with the direction of reported differences between conventional stainless steel and low-adhesion or liquid-infused surfaces, but it does not constitute kinetic calibration [10–12].

3.2. Finite-horizon biofilm response at the selected site

With the baseline coupling $D_{\text{uv}} = f_{\text{illum}} = 0.755556$ and $T = 240$ h, the terminal-window metrics obtained from the corrected scripts are (Table 2):

Table 2: Finite-horizon response at the selected site. The terminal-window averages use 241 samples from 216.0 to 240.0 h, inclusive.

Quantity	micro_SS	micro_LIS
$\overline{A}_T$	0.193555	0.030924
$\overline{B}_T$	5.233267×10^{-32}	5.034721×10^{-97}
$\log_{10}(\overline{B}_T)$	-31.281227	-96.298025
$\mathcal{C}_{\text{bio}}$	0	1

Both cases are in a negative-net-growth regime. The value $\mathcal{C}_{\text{bio}} = 0$ for micro_SS does not indicate uncontrolled biological accumulation; it indicates that micro_SS is the larger of two already vanishing finite-horizon responses under the pairwise normalization. The log-scale biomass and the critical-dose analysis are therefore more informative than the bounded index in this regime.

3.3. Critical-dose and biological sensitivity analysis

Solving $\lambda_B(D_c) = 0$ gives

$$\begin{aligned} D_c &= 0.396127 \quad \text{for micro\_SS}, \\ D_c &= 0.052941 \quad \text{for micro\_LIS}. \end{aligned} \tag{34}$$

The selected-site value $D_{\text{uv}} = 0.755556$ exceeds both thresholds. Figure 2 also shows that the sharp transition in the original dose-response sweep is an analytical consequence of the sign change in λ_B, not evidence of a measured sterilization threshold.

Table 3: One-at-a-time sensitivity of the critical normalized dose D_c to $\pm 20\%$ parameter perturbations. Each interval reports the minimum and maximum threshold generated by the two perturbations.

Quantity	micro_SS	micro_LIS
Baseline D_c	0.396127	0.052941
$\mu_{\max}$ interval	0.339–0.448	0.039–0.066
k_d interval	0.389–0.403	0.041–0.065
Φ_0 interval	0.362–0.426	0.043–0.061
β_ϕ interval	0.330–0.495	0.044–0.066

For micro_SS, β_ϕ produces the largest one-at-a-time threshold excursion, followed by $\mu_{\max}$ and Φ_0; k_d is less influential around the baseline. For micro_LIS, all four parameters materially affect the small threshold, with $\mu_{\max}$, k_d, and β_ϕ producing comparable relative shifts. The separation between the two baseline thresholds remains substantially larger than the perturbation intervals, preserving the relative SS–LIS ordering under this local sensitivity test (Table 3).

3.4. Geometry-energy and thermal sensitivities

At fixed aspect ratio $\kappa = h/R$, density, and specific process energy, Equation (6) gives

$$\frac{E_{\text{sint}}}{E_0} = \left(\frac{R}{R_0}\right)^2 \left(\frac{t}{t_0}\right). \tag{35}$$

Consequently, a 25% increase in base radius raises energy by 56.25%, whereas a 25% increase in thickness raises energy by 25%. Figure 3 shows this normalized trade-off without imposing an unsupported process efficiency or absolute shell size.

For the first-order thermal-resistance relation $\Delta T \propto qt/k$, the parameter sensitivities are (Table 4):

Table 4: First-order thermal-drop sensitivity for independent $\pm 25\%$ perturbations.

Perturbed quantity	-25%	$+25\%$
Thickness t	$0.75\Delta T_0$	$1.25\Delta T_0$
Conductivity k	$1.33\Delta T_0$	$0.80\Delta T_0$
Heat flux q	$0.75\Delta T_0$	$1.25\Delta T_0$

This scaling identifies conductivity uncertainty as asymmetric in its effect on thermal drop. It does not resolve transient three-dimensional heat bridges, penetrations, internal equipment, or radiative exchange among interior surfaces.

4. Discussion

The revision changes the interpretation of the biological output without changing the governing ordinary differential equations (ODEs). The large values previously described as steady states are finite-time exponential responses in the $\lambda_B > 0$ regime, whereas extremely small values occur when radiative damage makes $\lambda_B < 0$. Reporting $\overline{B}_T$, λ_B, and D_c distinguishes numerical horizon effects from equilibrium behavior. The critical-dose analysis shows a materially wider suppression margin for the LIS-like prior than for the SS-like prior, and the one-at-a-time perturbations do not reverse that ordering.

The dimensionless dose remains the largest limitation in connecting site illumination to biofilm response. Exterior illumination controls available electrical or optical power, but internal microbial exposure depends on source efficiency, duty cycle, attenuation, shielding, surface orientation, dust, and operational constraints. The coupling coefficient χ_{uv} makes this assumption explicit. A site with $f_{\text{illum}} = 0.756$ does not automatically impose $D_{\text{uv}} = 0.756$ on an internal liner; that equality is the baseline engineered-control scenario. Direct comparison with published ultraviolet-C (UVC) or ultraviolet-C light-emitting diode (UV-LED) inactivation experiments requires calibration of χ_{uv} against wavelength-resolved irradiance and exposure time [34–39].

The geometry-energy sensitivity is quantitative but normalized. It establishes that base radius is a stronger first-order energy driver than thickness because of the $R^2 t$ scaling, while the absolute construction budget remains dominated by E_s, density, porosity, heat loss, concentrator efficiency, and toolpath. Similarly, the thermal sensitivity table is a resistance-level diagnostic rather than a substitute for three-dimensional analysis. The radial model cannot represent local heat bridges at penetrations, asymmetric illumination, contact resistance, internal equipment, multilayer delamination, or azimuthal heat spreading.

Operational challenges remain outside the resolved state variables. Robotic emplacement and excavation are assumed feasible; dust mitigation is represented only by a constant derating factor; and liner degradation, abrasion, radiation aging, leakage, cleaning cycles, and surface-property drift are not modeled. The biological priors represent fixed surface states. Any degradation that changes roughness, wettability, lubricant retention, or optical transmission would require time-dependent Φ_0 and β_ϕ.

The OSD-554 transformation is transparent but weakly constrained. Selecting the ten largest absolute flight-to-ground fold changes and averaging normalized counts does not identify causal adhesion, growth, detachment,

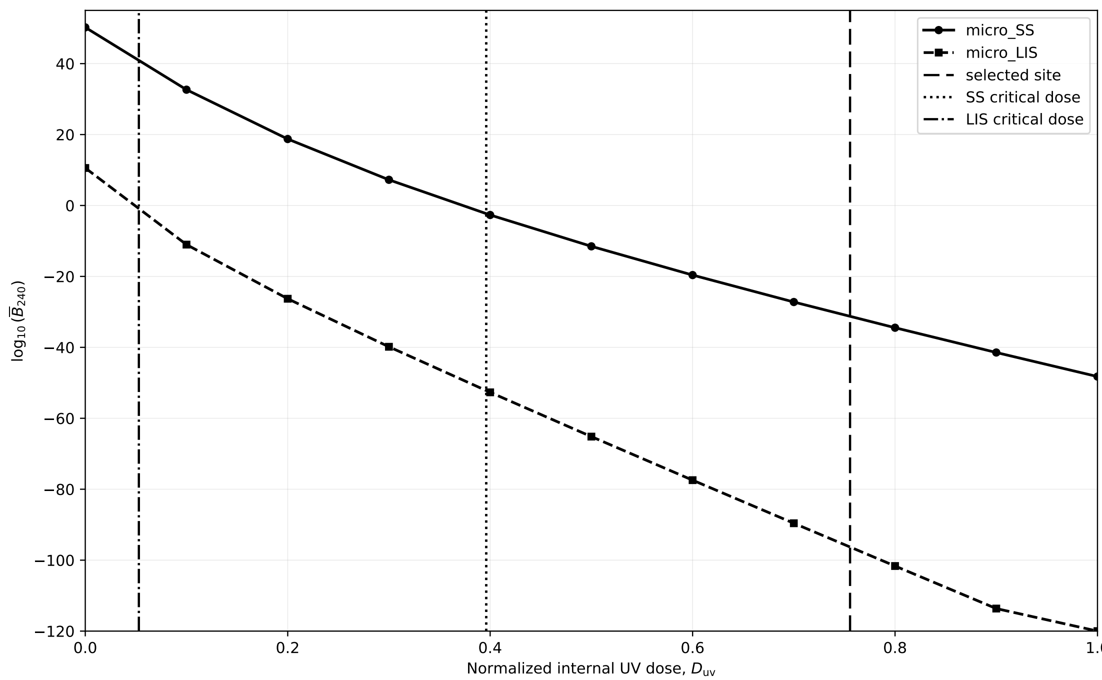

Figure 2: Finite-horizon biofilm response as a function of normalized internal UV dose. Biomass is averaged over the final 10% of a 240 h simulation. Values below 10^{-120} are clipped for visualization. Vertical lines identify the analytical critical doses and the selected-site dose. The horizontal axis is a normalized internal-control variable, not a directly calibrated lunar UV fluence.

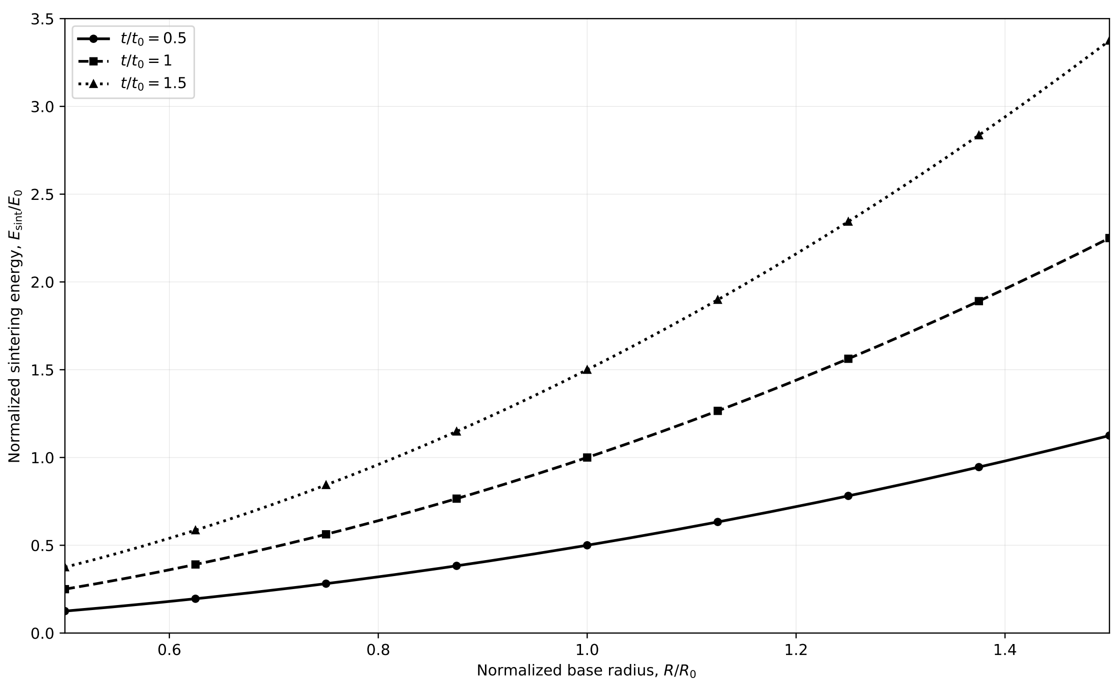

Figure 3: Normalized sintering-energy scaling for a spherical-cap shell at fixed rise-to-radius ratio. Energy varies quadratically with base radius and linearly with shell thickness. Absolute energy remains proportional to the uncertain specific process energy and processed-regolith density.

or UV-response parameters. The monotonic mapping supplies reproducible priors for comparative computation only. Experimental validation should therefore estimate parameters from replicated time-series measurements rather than from transcript abundance alone. A suitable campaign would cross material class, gravity analogue, temperature, nutrient level, humidity, and calibrated UV fluence, with independent fitting and held-out validation.

Within these limitations, the framework provides a reproducible front-end for eliminating clearly unfavorable combinations and defining the experiments or high-fidelity simulations needed next. Its defensible outputs are relative rankings, normalized scaling laws, uncertainty intervals, and explicit assumptions. Mission-level claims about structural safety, thermal habitability, sterilization, construction duration, or microbial risk are outside its present evidentiary scope.

5. Conclusions

The revised framework integrates spherical-cap geometry, polar illumination screening, radial thermal analysis, sintering-energy scaling, and finite-horizon biofilm dynamics without embedding source-code listings in the manuscript. The code is instead provided through an external reproducibility archive [40].

Two corrections are technically consequential. The thermal equation now uses the spherical $2/r$ term and absorbed solar flux is expressed with $(1 - \alpha_{\text{bol}})$. The biological output is no longer described as a positive steady state; the model is evaluated by a 240 h terminal-window biomass, the asymptotic net-growth exponent, and the critical normalized dose.

For the reported priors, $D_c = 0.396127$ for the SS-like liner and $D_c = 0.052941$ for the LIS-like liner. Under $\pm 20\%$ one-at-a-time parameter perturbations, the threshold intervals remain separated, preserving the qualitative material ordering. Normalized construction scaling gives $E_{\text{sint}} \propto R^2 t$ at fixed aspect ratio, while first-order thermal resistance gives $\Delta T \propto qt/k$.

These results support exploratory comparison and experimental design. They do not provide validated lunar-habitat performance, calibrated UV requirements, or operational biofilm-risk predictions. The next required step is joint physical and biological validation under controlled lunar-analogue boundary conditions.

Funding

This research received no external funding.

Acknowledgments

The author acknowledges the NASA Open Science Data Repository and NASA planetary-data archives for providing publicly accessible datasets used in this study. NASA had no involvement in the design, analysis, interpretation, or conclusions of this work.

Author contributions

Miguel Angel Vargas Cruz: Conceptualization, Methodology, Software, Validation, Formal analysis, Investigation, Data curation, Visualization, Writing—original draft, Writing—review and editing, and Project administration. The sole author has read and agreed to the submitted version of the manuscript.

Availability of Data and Materials

The data products and code used in this study are publicly available as follows:

LOLA topography. Provides the gridded digital-elevation and polar-topography products used for horizon and illumination screening [22].

Diviner thermophysical data. The NASA PDS data set provides the gridded thermal and thermophysical products used to constrain the thermal model [42].

LROC imaging. The NASA PDS bundle provides calibrated LROC images and local site context [43].

OSD-554 biological data. The NASA Open Science Data Repository (OSDR) study provides the normalized-count tables and study metadata used to construct the SS- and LIS-like biological priors [11].

Code archive. The external reproducibility archive contains the parametric shell renderer, planetary-data preprocessing, horizon and illumination analysis, biological-prior construction, biofilm integration, controllability-index calculation, dose-response sweep, module descriptions, and execution sequence [40].

All listed NASA records are accessible without charge. No access restrictions were encountered; reuse remains subject to the applicable repository terms and record-specific metadata.

AI-declaration

During revision of this manuscript, the author used OpenAI ChatGPT (GPT-5.6 Thinking) for English-language editing. The author reviewed and verified all AI-assisted content and takes full responsibility for the accuracy, integrity, and content of the manuscript.

conflicts of interest

The author declares no conflict of interest.

References

[1] E. Mazarico, G. A. Neumann, D. E. Smith, M. T. Zuber and M. H. Torrence, "Illumination conditions of the lunar polar regions using LOLA topography," *Icarus*, vol. 211, no. 2, pp. 1066-1081, 2011. DOI:10.1016/j.icarus.2010.10.030.

[2] P. Gläser, J. Oberst, G. A. Neumann, E. Mazarico, E. J. Speyerer and M. S. Robinson, "Illumination conditions at the lunar poles: Implications for future exploration," *Planetary and Space Science*, vol. 162, pp. 170-178, 2018. DOI:10.1016/j.pss.2017.07.006.

[3] P. O. Hayne, J. L. Bandfield, M. A. Siegler, A. R. Vasavada, R. R. Ghent, J. P. Williams, B. T. Greenhagen, O. Aharonson, C. M. Elder, P. G. Lucey and D. A. Paige, "Global Regolith Thermophysical Properties of the Moon From the Diviner Lunar Radiometer Experiment," *Journal of Geophysical Research: Planets*, vol. 122, no. 12, pp. 2371-2400, 2017. DOI:10.1002/2017JE005387.

[4] R. Zhang, T. Wang and G. Wang, "Review of lunar regolith forming technologies for in situ manufacturing/construction on the lunar surface," *Additive Manufacturing Frontiers*, vol. 4, no. 3, p. 200238, 2025. DOI:10.1016/j.amf.2025.200238.

[5] A. Meurisse, A. Makaya, C. Willsch and M. Sperl, "Solar 3D printing of lunar regolith," *Acta Astronautica*, vol. 152, pp. 800-810, 2018. DOI:10.1016/j.actaastro.2018.06.063.

[6] K. Baxter, E. Sas, K. Clark, M. Walsh, N. Pradeep, A. Batool, C. Naney, M. Vargas, N. Kennerdale, K. Das, Z. Shi, A. Kelam, V. Verma, M. Simões, D. Neefs, V. Ravichandran, M. Tirumalai, B. Barbero, G. Macori, E. Gonzalez, B. Sikes, F. Karouia and N. Brereton, "Biofilms: From the cradle of life to life support," *npj Biofilms Microbiomes*, 2026. DOI:10.1038/s41522-025-00875-8.

[7] A. A. Voorhies, C. Mark Ott, S. Mehta, D. L. Pierson, B. E. Crucian, A. Feiveson, C. M. Oubre, M. Torralba, K. Moncera, Y. Zhang, E. Zurek and H. A. Lorenzi, "Study of the impact of long-duration space missions at the International Space Station on the astronaut microbiome," *Scientific Reports*, vol. 9, no. 1, p. 9911, 2019. DOI:10.1038/s41598-019-46303-8.

[8] K. Landry, J. Morey, B. Bharat, N. Haney and S. Panesar, "Biofilms—Impacts on human health and its relevance to space travel," *Microorganisms*, vol. 8, no. 7, art. no. 998, 2020. DOI:10.3390/microorganisms8070998.

[9] R. A. Salido, H. N. Zhao, D. McDonald, H. Mannochio-Russo, S. Zuffa, R. E. Oles, A. T. Aron, Y. El Abiead, S. Farmer, A. González, C. Martino, I. Mohanty, C. W. Parker, L. Patel, P. W. Portal Gomes, R. Schmid, T. Schwartz, J. Zhu, M. R. Barratt, K. H. Rubins, H. Chu, F. Karouia, K. Venkateswaran, P. C. Dorrestein and R. Knight, "The International Space Station has a unique and extreme microbial and chemical environment driven by use patterns," *Cell*, vol. 188, no. 7, pp. 2022-2041.e23, 2025. DOI:10.1016/j.cell.2025.01.039.

[10] D. Goeres, Y. Velez, B. Kjellerup and R. McLean, "Biofilm and human spaceflight," *Biofilm*, vol. 6, p. 100150, 2023. DOI:10.1016/j.bioflm.2023.100150.

[11] "OSD-554. Characterization of Biofilm Formation, Growth, and Gene Expression on Different Materials and Environmental Conditions in Microgravity (Gene expression of Pseudomonas aeruginosa biofilms)," NASA OSDR, version 2, updated 26 March 2024. DOI:10.26030/d5dg-7s68. Available from: https://osdr.nasa.gov/bio/repo/data/studies/OSD-554.

[12] "Polymicrobial Biofilm Growth and Control during Spaceflight (Bacterial Adhesion and Corrosion)," NASA, 2023. Available from: https://science.nasa.gov/biological-physical/investigations/bacterial-adhesion/.

[13] S. Timoshenko and S. Woinowsky-Krieger, *Theory of plates and shells*. McGraw–Hill, 1964.

[14] V. Terzi and T. Makarios, "Finite Element In-Depth Verification: Base Displacements of a Spherical Dome Loaded by Edge Forces and Moments," *Modelling*, vol. 5, no. 1, pp. 37–54, 2024. DOI:10.3390/modelling5010003.

[15] S. Wood, "An Analytic Model for the Thermal Conductivity of Planetary Regolith: Uncemented, Non-Spherical Particulates," in *44th Lunar and Planetary Science Conference*, paper 3077, 2013.

[16] P. Gläser and D. Gläser, "Modeling near-surface temperatures of airless bodies with application to the Moon," *Astronomy & Astrophysics*, vol. 627, p. A129, 2019. DOI:10.1051/0004-6361/201935514.

[17] E. Mazarico, M. Barker and J. Nicholas, "Advanced illumination modeling for data analysis and calibration. Application to the Moon," *Advances in Space Research*, vol. 62, no. 11, pp. 3214-3228, 2018. DOI:10.1016/j.asr.2018.08.022.

[18] Y. Zhang, B. Liu, K. Di, S. Liu, Z. Yue, S. Han, J. Wang, W. Wan and B. Xie, "Analysis of Illumination Conditions in the Lunar South Polar Region Using Multi-Temporal High-Resolution Orbital Images," *Remote Sensing*, vol. 15, no. 24, art. no. 5691, 2023. DOI:10.3390/rs15245691.

[19] X. Tong, Q. Huang, S. Liu, H. Xie, H. Chen, Y. Wang, X. Xu, C. Wang and Y. Jin, "A high-precision horizon-based illumination modeling method for the lunar surface using pyramidal LOLA data," *Icarus*, vol. 390, p. 115302, 2023. DOI:10.1016/j.icarus.2022.115302.

[20] M. Barker, E. Mazarico, G. Neumann, D. Smith, M. Zuber and J. Head, "Improved LOLA elevation maps for south pole landing sites: Error estimates and their impact on illumination conditions," *Planetary and Space Science*, vol. 203, p. 105119, 2021. DOI:10.1016/j.pss.2020.105119.

[21] A. Ryan, D. Pino, M. Bernacki and M. Delbo, "Full-Field Modeling of Heat Transfer in Asteroid

Regolith: 1. Radiative Thermal Conductivity of Polydisperse Particulates," *Journal of Geophysical Research: Planets*, vol. 125, no. 2, 2020. DOI:10.1029/2019JE006100.

[22] "A New View of the Lunar South Pole from LOLA," NASA's Planetary Geology, Geophysics and Geochemistry Laboratory, 2020. Available from: https://pgda.gsfc.nasa.gov/products/90.

[23] M. Barker, E. Mazarico, G. Neumann, D. Smith, M. Zuber, J. Head and X. Sun, "A New View of the Lunar South Pole from the Lunar Orbiter Laser Altimeter (LOLA)," *The Planetary Science Journal*, vol. 4, no. 9, p. 183, Sep. 2023. DOI:10.3847/PSJ/acf3e1.

[24] K. Ogawa, N. Sakatani, Y. Iijima, M. Arakawa, R. Honda and S. Tanaka, "Thermal conductivity model for powdered materials under vacuum based on experimental studies," *AIP Advances*, vol. 7, no. 1, p. 015310, Jan. 2017. DOI:10.1063/1.4975153.

[25] S. Lim, J. Bowen, G. Degli-Alessandrini, M. Anand, A. Cowley and V. Levin Prabhu, "Investigating the microwave heating behaviour of lunar soil simulant JSC-1A at different input powers," *Scientific Reports*, vol. 11, no. 1, p. 2133, 2021. DOI:10.1038/s41598-021-81691-w.

[26] A. Gatto, S. Defanti, E. Bassoli, A. Mattioni, U. Martini and G. Incerti, "Preliminary study on localized microwave sintering of lunar regolith," *Acta Astronautica*, vol. 218, pp. 126-136, 2024. DOI:10.1016/j.actaastro.2024.02.026.

[27] E. Ethridge and W. Kaukler, "Microwave Extraction of Water from Lunar Regolith Simulant," *AIP Conference Proceedings*, vol. 880, no. 1, pp. 830-837, Jan. 2007. DOI:10.1063/1.2437523.

[28] S. Tsubaki, S. Fujii, M. Yamamoto, H. Kanamori, T. Hoshino, S. Hosoda and Y. Wada, "Self-Sufficient Production of Lunar Regolith Gravels on the Moon by Ultrarapid Microwave Sintering," *ACS Omega*, vol. 9, no. 20, 2024. DOI:10.1021/acsomega.4c02702.

[29] S. Tao, B. Vinh, N. Ceshkovsky and J. Chang, "MOONPads: Microwave-Sintering Operations Of Nanophase-Iron Pads," NASA Human Lander Challenge Technical Paper, 2024. Available from: https://hulc.nianet.org/wp-content/uploads/2024 -HuLC-Chart-Deck-University-of-Calififornia-San-Diego-MOON-Pads.pdf.

[30] H. Eberl, E. Morgenroth, D. Noguera, C. Picioreanu, B. Rittmann, M. van Loosdrecht and O. Wanner, *Mathematical Modelling of Biofilms*. IWA Publishing, 2006. ISBN: 9781780402482. DOI:10.2166/9781780402482.

[31] F. Abbas, "*Mathematical Contributions to One-Dimensional Biofilm Models*," Ph.D. thesis, University of Guelph, 2011.

[32] S. Skoneczny and M. Cioch-Skoneczny, "Approximate Models of Microbiological Processes in a Biofilm Formed on Fine Spherical Particles," *Processes*, vol. 10, no. 1, art. no. 48, 2022. DOI:10.3390/pr10010048.

[33] H. Eberl, C. Picioreanu, M. van Loosdrecht, J.J Heijnen and J. Kreft, "Mathematical Modelling of Biofilm Structures," *Antonie van Leeuwenhoek*, vol. 81, pp. 245–256, 2002. DOI:10.1023/A:1020527020464.

[34] T. Mullin, S. MacIsaac, A. Stoddart and G. Gagnon, "Impact of Material Properties for Improved Pseudomonas aeruginosa Biofilm Inactivation by UV-LEDs," *Scientific Reports*, vol. 15, 2025. DOI:10.1038/s41598-025-15192-5.

[35] S. Gora, K. Rauch, C. Ontiveros, A. Stoddart and G. Gagnon, "Inactivation of biofilm-bound Pseudomonas aeruginosa bacteria using UVC light emitting diodes (UVC LEDs)," *Water Research*, vol. 151, pp. 193-202, 2019. DOI:10.1016/j.watres.2018.12.021.

[36] B. Ma, S. Seyedi, E. Wells, D. McCarthy, N. Crosbie and K. Linden, "Inactivation of biofilm-bound bacterial cells using irradiation across UVC wavelengths," *Water Research*, vol. 217, p. 118379, 2022. DOI:10.1016/j.watres.2022.118379.

[37] S. Gora, B. Ma, M. Lanzarini-Lopes, H. Torkzadeh, Z. Zhao, C. Ley Matthews, P. Westerhoff, K. Linden, B. Barbeau, R. Simons, G. Gagnon, P. Di Falco and M. Mohsin, "Control of biofilms with UV light: a critical review of mechanisms and applications," *Environmental Science: Water Research & Technology*, vol. 10, no. 12, pp. 2205–2236, 2024. DOI:10.1039/D4EW00506F.

[38] M. Said, I. Daly, H. Nasr and A. Hassen, "Monitoring of Biofilm Production by Pseudomonas aeruginosa after UVC Irradiation: Dose/Response Modelling," *Annals of Microbiology*, vol. 63, 2013. DOI:10.1007/s13213-012-0487-7.

[39] C. Jones, S. Valdeig, R. Sova and C. Weiss, "Inside-out Ultraviolet-C Sterilization of Pseudomonas aeruginosa Biofilm In Vitro," *Photochemistry and Photobiology*, vol. 92, no. 6, pp. 835-841, 2016. DOI:10.1111/php.12637.

[40] M. A. Vargas Cruz, "Code for Architecture of Sintered-Regolith Lunar Polar Microhabitats for Biofilm Research", 2026. Available from: https:// www.miguelangelvargascruz.com/codeforarchitectureofsinteredregolit blog_6340.html.

[41] G. A. Neumann, "LRO Moon Laser Altimeter 4 Gridded Data Records V1.0," NASA Planetary Data System, data set `LRO-L-LOLA-4-GDR-V1.0`, version 1.0, released 15 December 2015. DOI:10.17189/1520642.

[42] D. A. Paige et al., "LRO Diviner Lunar Radiometer Experiment Level 5 Gridded Data Records V1.0," NASA Planetary Data System, data set `LRO-L-DLRE-5-GDR-V1.0`, version 1.0, released 15 December 2017. DOI:10.17189/1520647.

[43] Lunar Reconnaissance Orbiter Camera Science Operations Center, "LRO LROC Data Archive," NASA Planetary Data System, bundle `urn:nasa:pds:lro-l-lroc-5-rdr::3.0`, version 3.0, 2023. DOI:10.17189/a6a1-mw73.